
ANL/MCS-TM-381

# Implementation and Validation of Photon Transport in OpenMC

Mathematics and Computer Science Division

ANL/MCS-TM-381

# Implementation and Validation of Photon Transport in OpenMC

prepared by
Amanda L. Lund and Paul K. Romano

Mathematics and Computer Science Division

December 14, 2018

# 1 Introduction

OpenMC is a Monte Carlo particle transport code focused on reactor physics calculations. It stochastically simulates neutrons moving through 3D models using constructive solid geometry and continuous-energy cross sections. Recently, a photon transport capability was added to OpenMC. In reactor simulations, photon transport is needed, for example, to account for photon heating: although the majority of the energy deposited at a fission site comes from the kinetic energy of the fission fragments, a nontrivial portion can be carried away by photons. Therefore, photons produced in neutron reactions must be simulated in order to accurately model energy deposition.

OpenMC can now simulate neutron-induced photon production as well as perform pure photon calculations. The four basic photon interactions with matter — coherent (Rayleigh) scattering, incoherent (Compton) scattering, the photoelectric effect, and pair production — are modeled. Secondary processes that can create new photons (i.e., atomic relaxation, electron-positron annihilation, and bremsstrahlung) are also included. The methods implemented here were validated against MCNP6 for a variety of materials and energies.

# 2 Photon Physics

Photons, being neutral particles, behave in much the same manner as neutrons, traveling in straight lines and experiencing occasional collisions that change their energy and direction. Since the transport of a photon follows the same logic as does the transport of a neutron, the focus here is on the implementation of the photon physics. Some assumptions are made in the methodology: the photons are considered to be unpolarized, and interactions are assumed to occur with free atoms, meaning the macroscopic cross sections can be approximated as the sum of the cross sections of the atomic constituents. Because photon interactions depend on material properties below $\sim 1$ keV, this is typically the cutoff energy used in photon calculations to ensure that the free atom model remains valid. The data needed to model photon interactions and photon production comes primarily from ENDF sublibraries, but additional sources are needed in some cases.

## 2.1 Photon Interactions

OpenMC models the four main photon interactions with matter for energies between 1 keV and 10 GeV and for Z = 1 – 98. The methodology used is discussed below.

### 2.1.1 Coherent (Rayleigh) Scattering

The elastic scattering of a photon off a free charged particle is known as Thomson scattering. The differential cross section is independent of the energy of the incident photon and is given by

$$\frac{d\sigma}{d\mu} = \pi r_e^2 (1 + \mu^2), \tag{1}$$

where $\mu$ is the cosine of the scattering angle and $r_e$ is the classical electron radius. Thomson scattering can occur when the photon energy is much less than the rest mass energy of the particle.

In practice, most elastic scattering of photons off electrons happens not with free electrons but with those bound in atoms. This process is known as Rayleigh scattering. The radiation scattered off individual bound electrons combines coherently, so Rayleigh scattering is also referred to as coherent scattering.

The differential cross section for Rayleigh scattering can be formulated by extending the Thompson cross section using form factors to account for bound electrons:

$$\begin{aligned}\frac{d\sigma(E,E',\mu)}{d\mu} &= \pi r_e^2(1+\mu^2)\ \left|F(x,Z)+F'+iF''\right|^2 \\ &= \pi r_e^2(1+\mu^2)\left[(F(x,Z)+F'(E))^2+F''(E)^2\right],\end{aligned} \tag{2}$$

where $F(x,Z)$ is a form factor as a function of the momentum transfer $x$ and the atomic number $Z$ and the term $F'+iF''$ accounts for anomalous scattering that can occur near absorption edges [1]. In a Monte Carlo simulation, when a photon undergoes coherent scattering, its energy does not change, so only the scattering angle needs to be sampled using the differential cross section in Eq. (2). In OpenMC, as in most other Monte Carlo codes, anomalous scattering is ignored and Eq. (2) becomes

$$\frac{d\sigma(E,E',\mu)}{d\mu} = \pi r_e^2(1+\mu^2)F(x,Z)^2. \tag{3}$$

In order to construct a proper probability density, the differential cross section in Eq. (3) must be normalized by the integrated coherent scattering cross section, resulting in

$$p(\mu)d\mu = \frac{\pi r_e^2}{\sigma(E)}(1+\mu^2)F(x,Z)^2 d\mu. \tag{4}$$

Since the form factor is given in terms of the momentum transfer, it is more convenient to change variables of the probability density to $x^2$. The momentum transfer is traditionally expressed as

$$x = ak\sqrt{1-\mu}, \tag{5}$$

where $k$ is the ratio of the photon energy to the electron rest mass and the coefficient $a$ is given by

$$a = \frac{m_e c^2}{\sqrt{2}hc} \approx 29.14329\ \text{Å}, \tag{6}$$

where $m_e$ is the mass of the electron, $c$ is the speed of light in a vacuum, and $h$ is Planck's constant. Using Eq. (5), one can show that $\mu = 1-[x/(ak)]^2$ and $d\mu/dx^2 = -1/(ak)^2$. The probability density in $x^2$ is

$$p(x^2)dx^2 = p(\mu)\left|\frac{d\mu}{dx^2}\right|dx^2 = \frac{2\pi r_e^2 A(\bar{x}^2,Z)}{(ak)^2\sigma(E)}\left(\frac{1+\mu^2}{2}\right)\left(\frac{F(x,Z)^2}{A(\bar{x}^2,Z)}\right)dx^2, \tag{7}$$

where $\bar{x}$ is the maximum value of $x$ (at $\mu = -1$),

$$\bar{x} = ak\sqrt{2} = \frac{m_e c^2}{hc} k, \tag{8}$$

and $A(x^2, Z)$ is the integral of the square of the form factor,

$$A(x^2, Z) = \int_0^{x^2} F(x', Z)^2 dx'^2. \tag{9}$$

Multiplying and dividing the probability density by Eq. (9), one can express the density in Eq. (7) as the product of the two separate densities in parentheses. In OpenMC, a table of $A(x^2, Z)$ versus $x^2$ is pregenerated and used at runtime to do a table search on the cumulative distribution function,

$$\frac{\int_0^{x^2} F(x', Z)^2 dx'^2}{\int_0^{\bar{x}^2} F(x', Z)^2 dx'^2}. \tag{10}$$

Once a trial $x^2$ has been selected, $\mu$ can be calculated, and rejection sampling can be performed by using the Thomson scattering differential cross section. The complete algorithm is as follows:

1. Determine $\bar{x}^2$ using Eq. (8).
2. Determine $A_{max} = A(\bar{x}^2, Z)$ using the pregenerated tabulated data.
3. Sample the cumulative density by calculating $A' = \xi_1 A_{max}$, where $\xi_1$ is a uniformly distributed random number.
4. Perform a binary search to determine the value of $x^2$ that satisfies $A(x^2, Z) = A'$.
5. Using Eq. (5) and Eq. (8), calculate $\mu = 1 - 2x^2/\bar{x}^2$.
6. If $\xi_2 < (1 + \mu^2)/2$, accept $\mu$. Otherwise, repeat the sampling from step 3.

### 2.1.2 Incoherent (Compton) Scattering

The Thomson cross section describes photons scattering off free electrons using classical electromagnetism. It is valid only in the low energy limit and fails to explain differences in wavelength between the incident and scattered radiation. The differential cross section for photon scattering off free electrons that is valid for all energies can be found by using quantum electrodynamics and is known as the Klein-Nishina formula:

$$\frac{d\sigma_{KN}}{d\mu} = \pi r_e^2 \left(\frac{k'}{k}\right)^2 \left[\frac{k'}{k} + \frac{k}{k'} + \mu^2 - 1\right], \tag{11}$$

where $k$ and $k'$ are the ratios of the incoming and exiting photon energies to the electron rest mass energy equivalent (0.511 MeV), respectively. Although the outgoing energy and angle

appear to be separate, actually a one-to-one relationship exists between them such that only one needs to be sampled:

$$k' = \frac{k}{1 + k(1-\mu)}. \tag{12}$$

Note that when $k'/k$ goes to one, that is, the scattering is elastic, the Klein-Nishina cross section becomes identical to the Thomson cross section. In general, however, the scattering is inelastic and is known as Compton scattering.

When a photon interacts with a bound electron in an atom, the Klein-Nishina formula must be modified to account for the binding effects. As with coherent scattering, this is done by using a form factor. The differential cross section for incoherent scattering is given by

$$\frac{d\sigma}{d\mu} = \frac{d\sigma_{KN}}{d\mu} S(x, Z) = \pi r_e^2 \left(\frac{k'}{k}\right)^2 \left[\frac{k'}{k} + \frac{k}{k'} + \mu^2 - 1\right] S(x, Z), \tag{13}$$

where $S(x, Z)$ is the form factor. The approach in OpenMC is to first sample the Klein-Nishina cross section and then perform rejection sampling on the form factor. As in other codes, Kahn's rejection method [2] is used for $k < 3$ and a direct method by Koblinger [3] is used for $k \geq 3$. The complete algorithm is as follows:

1. If $k < 3$, sample $\mu$ from the Klein-Nishina cross section using Kahn's rejection method. Otherwise, use Koblinger's direct method.

2. Calculate $x$ and $\bar{x}$ using Eq. (5) and Eq. (8), respectively.

3. If $\xi < S(x, Z)/S(\bar{x}, Z)$, accept $\mu$. Otherwise repeat from step 1.

Bound electrons are not at rest but have a momentum distribution that will cause the energy of the scattered photon to be Doppler broadened. More tightly bound electrons have a wider momentum distribution, so the energy spectrum of photons scattering off inner shell electrons will be broadened the most. In addition, scattering from bound electrons places a limit on the maximum scattered photon energy:

$$E'_{\max} = E - E_{b,i}, \tag{14}$$

where $E_{b,i}$ is the binding energy of the $i$th subshell.

Compton profiles $J_i(p_z)$ are used to account for the binding effects. The quantity $p_z = \mathbf{p} \cdot \mathbf{q}/q$ is the projection of the initial electron momentum on $\mathbf{q}$, where the scattering vector $\mathbf{q} = \mathbf{p} - \mathbf{p}'$ is the momentum gained by the photon, $\mathbf{p}$ is the initial momentum of the electron, and $\mathbf{p}'$ is the momentum of the scattered electron. Applying the conservation of energy and momentum, one can write $p_z$ in terms of the photon energy and scattering angle:

$$p_z = \frac{E - E' - EE'(1-\mu)/(m_e c^2)}{-\alpha\sqrt{E^2 + E'^2 - 2EE'\mu}}, \tag{15}$$

where $\alpha$ is the fine structure constant. The maximum momentum transferred, $p_{z,\max}$, can be calculated from Eq. (15) by using $E' = E'_{\max}$. The Compton profile of the $i$th electron subshell is defined as

$$J_i(p_z) = \int \int \rho_i(\mathbf{p}) dp_x dp_y, \tag{16}$$

where $\rho_i(\mathbf{p})$ is the initial electron momentum distribution. $J_i(p_z)$ can be interpreted as the probability density function of $p_z$.

The Doppler broadened energy of the Compton-scattered photon can be sampled by selecting an electron shell, sampling a value of $p_z$ using the Compton profile, and calculating the scattered photon energy. The theory and methodology used are described in detail in [4] and [5]. Compton profiles have been calculated by Biggs et al. [6] for $Z = 1-102$ and are available in the Geant4 G4EMLOW data file. The sampling algorithm is summarized below:

1. Sample $\mu$ from Eq. (13) using the algorithm described above.
2. Sample the electron subshell $i$ using the number of electrons per shell as the probability mass function.
3. Sample $p_z$ using $J_i(p_z)$ as the PDF.
4. Calculate $E'$ by solving Eq. (15) for $E'$ using the sampled value of $p_z$.
5. If $p_z < p_{z,\max}$ for shell $i$, accept $E'$. Otherwise repeat from step 2.

Because the Compton-scattered photons can transfer a large fraction of their energy to the kinetic energy of the recoil electron, which may in turn go on to lose its energy as bremsstrahlung radiation, one must accurately model the angular and energy distributions of Compton electrons. The energy of the recoil electron ejected from the $i$th subshell is given by

$$E_- = E - E' - E_{b,i}. \tag{17}$$

The direction of the electron is assumed to be in the direction of the momentum transfer, with the cosine of the polar angle given by

$$\mu_- = \frac{E - E'\mu}{\sqrt{E^2 + E'^2 - 2EE'\mu}} \tag{18}$$

and the azimuthal angle $\phi_- = \phi + \pi$, where $\phi$ is the azimuthal angle of the photon. The vacancy left by the ejected electron is filled through atomic relaxation.

### 2.1.3 Photoelectric Effect

In the photoelectric effect, the incident photon is absorbed by an atomic electron, which is then emitted from the $i$th shell with kinetic energy

$$E_- = E - E_{b,i}. \tag{19}$$

Photoelectric emission is possible only when the photon energy exceeds the binding energy of the shell. These binding energies are often referred to as edge energies because the otherwise continuously decreasing cross section has discontinuities at these points, creating the characteristic sawtooth shape. The photoelectric effect dominates at low energies and is more important for heavier elements.

When simulating the photoelectric effect, the first step is to sample the electron shell. The shell $i$ where the ionization occurs can be considered a discrete random variable with probability mass function

$$p_i = \frac{\sigma_{\text{pe},i}}{\sigma_{\text{pe}}}, \tag{20}$$

where $\sigma_{\text{pe},i}$ is the cross section of the $i$th shell and the total photoelectric cross section of the atom, $\sigma_{\text{pe}}$, is the sum over the shell cross sections. Once the shell has been sampled, the energy of the photoelectron is calculated by using Eq. (19). Atomic and shell cross sections from the ENDF/B-VII.1 photo-atomic sublibrary are used to simulate the photoelectric effect in OpenMC.

To determine the direction of the photoelectron, we implement the method described in [7], which models the angular distribution of the photoelectrons using the K-shell cross section derived by Sauter (K-shell electrons are the most tightly bound, and they contribute the most to $\sigma_{\text{pe}}$). The nonrelativistic Sauter distribution for unpolarized photons can be approximated as

$$\frac{d\sigma_{\text{pe}}}{d\mu_-} \propto \frac{1-\mu_-^2}{(1-\beta_-\mu_-)^4}, \tag{21}$$

where $\beta_-$ is the ratio of the velocity of the electron to the speed of light,

$$\beta_- = \frac{\sqrt{(E_-(E_- + 2m_e c^2)}}{E_- + m_e c^2}. \tag{22}$$

To sample $\mu_-$ from the Sauter distribution, we first express Eq. (21) in the form

$$f(\mu_-) = \frac{3}{2}\psi(\mu_-)g(\mu_-), \tag{23}$$

where

$$\psi(\mu_-) = \frac{(1-\beta_-^2)(1-\mu_-^2)}{(1-\beta_-\mu_-)^2}, \tag{24}$$

$$g(\mu_-) = \frac{1-\beta_-^2}{2(1-\beta_-\mu_-)^2}. \tag{25}$$

In the interval $[-1,1]$, $g(\mu_-)$ is a normalized PDF and $\psi(\mu_-)$ satisfies the condition $0 < \psi(\mu_-) < 1$. The following algorithm can now be used to sample $\mu_-$:

1. Using the inverse transform method, sample $\mu_-$ from $g(\mu_-)$ using the sampling formula
$$\mu_- = \frac{2\xi_1 + \beta_- - 1}{2\beta_-\xi_1 - \beta_- + 1}.$$
2. If $\xi_2 \leq \psi(\mu_-)$, accept $\mu_-$. Otherwise, repeat the sampling from step 1.

The azimuthal angle is sampled uniformly on $[0, 2\pi)$. The atom is left in an excited state with a vacancy in the $i$th shell and decays to its ground state through a cascade of transitions that produce fluorescent photons and Auger electrons.

### 2.1.4 Pair Production

In electron-positron pair production, a photon is absorbed in the vicinity of an atomic nucleus or an electron and an electron and positron are created. Pair production is the dominant interaction with matter at high photon energies and is more important for high-Z elements. When it takes place in the field of a nucleus, energy is essentially conserved among the incident photon and the resulting charged particles. Therefore, in order for pair production to occur, the photon energy must be greater than the sum of the rest mass energies of the electron and positron; in other words, $E_{\text{threshold,pp}} = 2m_e c^2 = 1.022$ MeV.

The photon can also interact in the field of an atomic electron. This process is referred to as "triplet production" because the target electron is ejected from the atom and three charged particles emerge from the interaction. In this case, the recoiling electron also absorbs some energy, so the energy threshold for triplet production is greater than that of pair production from atomic nuclei, with $E_{\text{threshold,tp}} = 4m_e c^2 = 2.044$ MeV. The ratio of the triplet production cross section to the pair production cross section is approximately 1/Z, so triplet production becomes increasingly unimportant for high-Z elements. Although it can be significant in lighter elements, the momentum of the recoil electron becomes negligible in the energy regime where pair production dominates. For our purposes, it is a good approximation to treat triplet production as pair production and simulate only the electron-positron pair.

Accurately modeling the creation of electron-positron pair is important because the charged particles can go on to lose much of their energy as bremsstrahlung radiation, and the subsequent annihilation of the positron with an electron produces two additional photons. We sample the energy and direction of the charged particles using a semiempirical model described in [8]. The Bethe-Heitler differential cross section, given by

$$\frac{d\sigma_{\text{pp}}}{d\epsilon} = \alpha r_e^2 Z^2 \left[ (\epsilon^2 + (1-\epsilon)^2)(\Phi_1 - 4f_C) + \frac{2}{3}\epsilon(1-\epsilon)(\Phi_2 - 4f_C) \right], \tag{26}$$

is used as a starting point, where $\alpha$ is the fine structure constant, $f_C$ is the Coulomb correction function, $\Phi_1$ and $\Phi_2$ are screening functions, and $\epsilon = (E_- + m_e c^2)/E$ is the electron reduced energy (i.e., the fraction of the photon energy given to the electron). $\epsilon$ can take values between $\epsilon_{\text{min}} = k^{-1}$ (when the kinetic energy of the electron is zero) and $\epsilon_{\text{max}} = 1 - k^{-1}$ (when the kinetic energy of the positron is zero). The Coulomb correction, given by

$$\begin{aligned} f_C = \alpha^2 Z^2 \big[ & (1+\alpha^2 Z^2)^{-1} + 0.202059 - 0.03693\alpha^2 Z^2 + 0.00835\alpha^4 Z^4 \\ & - 0.00201\alpha^6 Z^6 + 0.00049\alpha^8 Z^8 - 0.00012\alpha^{10} Z^{10} + 0.00003\alpha^{12} Z^{12} \big], \end{aligned} \tag{27}$$

is introduced to correct for the fact that the Bethe-Heitler differential cross section was derived by using the Born approximation, which treats the Coulomb interaction as a small perturbation.

The screening functions $\Phi_1$ and $\Phi_2$ account for the screening of the Coulomb field of the atomic nucleus by outer electrons. Since they are given by integrals that include the atomic form factor, they must be computed numerically for a realistic form factor. However, by assuming exponential screening and using a simplified form factor, analytical approximations of the screening functions can be derived:

$$\Phi_1 = 2 - 2\ln(1+b^2) - 4b\arctan(b^{-1}) + 4\ln(Rm_e c/\hbar) \tag{28}$$

$$\Phi_2 = \frac{4}{3} - 2\ln(1+b^2) + 2b^2\left[4 - 4b\arctan(b^{-1}) - 3\ln(1+b^{-2})\right] + 4\ln(Rm_e c/\hbar), \tag{29}$$

where

$$b = \frac{Rm_e c}{2k\epsilon(1-\epsilon)\hbar} \tag{30}$$

and $R$ is the screening radius. A table of values of the so-called reduced screening radius $Rm_e c/\hbar$ is provided by [8] for $Z = 1-99$.

The differential cross section in Eq. (26) with the approximations described above will not be accurate at low energies: the lower boundary of $\epsilon$ will be shifted above $\epsilon_{\min}$, and the upper boundary of $\epsilon$ will be shifted below $\epsilon_{\max}$. A correcting factor,

$$\begin{aligned} F_0(k,Z) = {} & (0.1774 + 12.10\alpha Z - 11.18\alpha^2 Z^2)(2/k)^{1/2} \\ & + (8.523 + 73.26\alpha Z - 44.41\alpha^2 Z^2)(2/k) \\ & - (13.52 + 121.1\alpha Z - 96.41\alpha^2 Z^2)(2/k)^{3/2} \\ & + (8.946 + 62.05\alpha Z - 63.41\alpha^2 Z^2)(2/k)^2, \end{aligned} \tag{31}$$

is introduced in order to offset this behavior. In order to aid sampling, the differential cross section used to sample $\epsilon$ (minus the normalization constant) can now be expressed in the form

$$\frac{d\sigma_{\text{pp}}}{d\epsilon} = u_1 \frac{\phi_1(\epsilon)}{\phi_1(1/2)}\pi_1(\epsilon) + u_2 \frac{\phi_2(\epsilon)}{\phi_2(1/2)}\pi_2(\epsilon), \tag{32}$$

where

$$u_1 = \frac{2}{3}\left(\frac{1}{2} - \frac{1}{k}\right)^2 \phi_1(1/2), \tag{33}$$

$$u_2 = \phi_2(1/2), \tag{34}$$

$$\phi_1(\epsilon) = \frac{1}{2}(3\Phi_1 - \Phi_2) - 4f_C(Z) + F_0(k,Z), \tag{35}$$

$$\phi_2(\epsilon) = \frac{1}{4}(3\Phi_1 + \Phi_2) - 4f_C(Z) + F_0(k,Z), \tag{36}$$

and

$$\pi_1(\epsilon) = \frac{3}{2}\left(\frac{1}{2} - \frac{1}{k}\right)^{-3}\left(\frac{1}{2} - \epsilon\right)^2, \tag{37}$$

$$\pi_2(\epsilon) = \frac{1}{2}\left(\frac{1}{2} - \frac{1}{k}\right)^{-1}. \tag{38}$$

The functions in Eq. (35) are non-negative and maximum at $\epsilon = 1/2$. In the interval $(\epsilon_{\min}, \epsilon_{\max})$, the functions in Eq. (37) are normalized PDFs and $\phi_i(\epsilon)/\phi_i(1/2)$ satisfies the condition $0 < \phi_i(\epsilon)/\phi_i(1/2) < 1$. The following algorithm can now be used to sample the reduced electron energy $\epsilon$:

1. Sample $i$ according to the point probabilities $p(i=1) = u_1/(u_1+u_2)$ and $p(i=2) = u_2/(u_1+u_2)$.

2. Using the inverse transform method, sample $\epsilon$ from $`\pi_i(\epsilon)$ using the sampling formula

$$\epsilon = \frac{1}{2} + \left(\frac{1}{2} - \frac{1}{k}\right)(2\xi_1 - 1)^{1/3} \qquad \text{if } i = 1$$
$$\epsilon = \frac{1}{k} + \left(\frac{1}{2} - \frac{1}{k}\right)2\xi_1 \qquad \text{if } i = 2.$$

3. If $\xi_2 \leq \phi_i(\epsilon)/\phi_i(1/2)$, accept $\epsilon$. Otherwise, repeat the sampling from step 1.

Because charged particles have a much smaller range than the mean free path of photons and because they immediately undergo multiple scattering events that randomize their direction, a simplified model is sufficient for sampling the direction of the electron and positron. The cosines of the polar angles are sampled by using the leading order term of the Sauter–Gluckstern–Hull distribution,

$$p(\mu_\pm) = C(1 - \beta_\pm \mu_\pm)^{-2}, \tag{39}$$

where $C$ is a normalization constant and $\beta_\pm$ is the ratio of the velocity of the charged particle to the speed of light given in Eq. (22). The inverse transform method is used to sample $\mu_-$ and $\mu_+$ from Eq. (39), by using the sampling formula

$$\mu_\pm = \frac{2\xi - 1 + \beta_\pm}{(2\xi - 1)\beta_\pm + 1}. \tag{40}$$

The azimuthal angles for the electron and positron are sampled independently and uniformly on $[0, 2\pi)$.

## 2.2 Secondary Processes

In addition to the four primary interactions with matter, all processes apart from coherent scattering can lead to the excitation/ionization of atoms. The de-excitation of these atoms may result in the emission of additional photons and of electrons and positrons that can themselves go on to produce photons through bremsstrahlung.

A Compton-scattered photon transfers a portion of its energy to the kinetic energy of the recoil electron, which in turn may lose the energy as bremsstrahlung radiation. The vacancy left in the shell by the ejected electron is filled through atomic relaxation, creating a shower of electrons and fluorescence photons. Similarly, the vacancy left by the electron emitted in the photoelectric effect is filled through atomic relaxation. Pair production generates an electron and a positron, both of which can emit bremsstrahlung radiation before the positron eventually collides with an electron, resulting in annihilation of the pair and the creation of two additional photons. Any secondary particles created during the simulation are stored in a secondary particle bank and transported immediately after the original particle history has terminated.

### 2.2.1 Atomic Relaxation

When an electron is ejected from an atom and a vacancy is left in an inner shell, an electron from a higher energy level will fill the vacancy. This results in either a radiative transition, in which a photon with a characteristic energy (fluorescence photon) is emitted, or nonradiative transition, in which an electron from a shell that is farther out (Auger electron) is emitted. If a nonradiative transition occurs, the new vacancy is filled in the same manner; as the process repeats, a shower of photons and electrons can be produced.

The energy of a fluorescence photon is equal to the energy difference between the transition states,

$$E = E_{b,v} - E_{b,i}, \tag{41}$$

where $E_{b,v}$ is the binding energy of the vacancy shell and $E_{b,i}$ is the binding energy of the shell from which the electron transitioned. The energy of an Auger electron is given by

$$E_{-} = E_{b,v} - E_{b,i} - E_{b,a}, \tag{42}$$

where $E_{b,a}$ is the binding energy of the shell from which the Auger electron is emitted. While Auger electrons are low energy so their range and bremsstrahlung yield is small, fluorescence photons can travel far before depositing their energy, so the relaxation process should be modeled in detail.

The data needed to simulate atomic relaxation (transition probabilities, binding energies, and the number of electrons in each subshell) is taken from the ENDF/B-VII.1 atomic relaxation sublibrary. Starting with the initial shell vacancy, the following recursive algorithm is used to fill vacancies and create fluorescence photons and Auger electrons:

1. If there are no transitions for the vacancy shell, create a fluorescence photon assuming it is from a captured free electron and terminate.

2. Sample a transition using the transition probabilities for the vacancy shell as the probability mass function.

3. Create either a fluorescence photon or Auger electron, sampling the direction of the particle isotropically.

4. If a nonradiative transition occurred, repeat from step 1 for the vacancy left by the emitted Auger electron.

5. Repeat from step 1 for the vacancy left by the transition electron.

### 2.2.2 Electron-Positron Annihilation

When a positron collides with an electron, both particles are annihilated, and generally two photons with equal energy are created. If the kinetic energy of the positron is high enough, the two photons can have different energies, and the higher-energy photon is emitted preferentially in the direction of flight of the positron. It is also possible to produce a single photon if the interaction occurs with a bound electron, and in some cases three (or, rarely, even more) photons

can be emitted. However, the annihilation cross section is largest for low-energy positrons; and as the positron energy decreases, the angular distribution of the emitted photons becomes isotropic.

In OpenMC, we assume the most likely case in which a low-energy positron (which has already lost most of its energy to bremsstrahlung radiation) interacts with an electron that is free and at rest. Two photons with energy equal to the electron rest mass energy $m_e c^2 = 0.511$ MeV are emitted isotropically in opposite directions.

### 2.2.3 Bremsstrahlung

When a charged particle is decelerated in the field of an atom, some of its kinetic energy is converted into electromagnetic radiation known as bremsstrahlung, or "braking radiation". In each event, an electron or positron with kinetic energy $T$ generates a photon with an energy $E$ between 0 and $T$. Bremsstrahlung is described by a cross section that is differential in photon energy, in the direction of the emitted photon, and in the final direction of the charged particle. In Monte Carlo simulations, however, one typically integrates over the angular variables to obtain a single differential cross section with respect to photon energy, which is often expressed in the form

$$\frac{d\sigma_{\text{br}}}{dE} = \frac{Z^2}{\beta^2}\frac{1}{E}\chi(Z, T, \kappa), \tag{43}$$

where $\kappa = E/T$ is the reduced photon energy and $\chi(Z, T, \kappa)$ is the scaled bremsstrahlung cross section, which is experimentally measured.

Because electrons are attracted to atomic nuclei whereas positrons are repulsed, the cross section for positrons is smaller, although it approaches that of electrons in the high-energy limit. To obtain the positron cross section, we multiply Eq. (43) by the $\kappa$-independent factor used in [8],

$$\begin{aligned} F_{\text{p}}(Z, T) =& 1 - \exp(-1.2359 \times 10^{-1} t + 6.1274 \times 10^{-2} t^2 - 3.1516 \times 10^{-2} t^3 & (44)\\ &+ 7.7446 \times 10^{-3} t^4 - 1.0595 \times 10^{-3} t^5 + 7.0568 \times 10^{-5} t^6 & (45)\\ &- 1.8080 \times 10^{-6} t^7), & (46) \end{aligned}$$

where

$$t = \ln\left(1 + \frac{10^6}{Z^2}\frac{T}{\text{m}_\text{e} c^2}\right). \tag{47}$$

$F_{\text{p}}(Z, T)$ is the ratio of the radiative stopping powers for positrons and electrons. Stopping power describes the average energy loss per unit path length of a charged particle as it passes through matter:

$$-\frac{dT}{ds} = n \int E \frac{d\sigma}{dE} dE \equiv S(T), \tag{48}$$

where $n$ is the number density of the material and $d\sigma/dE$ is the cross section differential in energy loss. The total stopping power $S(T)$ can be separated into two components: the

radiative stopping power $S_{\text{rad}}(T)$, which refers to the energy loss due to bremsstrahlung, and the collision stopping power $S_{\text{col}}(T)$, which refers to the energy loss due to inelastic collisions with bound electrons in the material that result in ionization and excitation. To obtain the radiative stopping power for positrons, we multipy the radiative stopping power for electrons by Eq. (44). Currently, the collision stopping power for electrons is also used for positrons.

While the models for photon interactions with matter described above can safely assume interactions occur with free atoms, sampling the target atom based on the macroscopic cross sections, molecular effects cannot necessarily be disregarded for charged particle treatment. For compounds and mixtures, the bremsstrahlung cross section is calculated by using Bragg's additivity rule as

$$\frac{d\sigma_{\text{br}}}{dE} = \frac{1}{\beta^2 E} \sum_i \gamma_i Z_i^2 \chi(Z_i, T, \kappa), \tag{49}$$

where the sum is over the constituent elements and $\gamma_i$ is the atomic fraction of the $i$th element. Similarly, the radiative stopping power is calculated by using Bragg's additivity rule as

$$S_{\text{rad}}(T) = \sum_i w_i S_{\text{rad},i}(T), \tag{50}$$

where $w_i$ is the mass fraction of the $i$th element. The collision stopping power, however, is a function of certain quantities such as the mean excitation energy $I$ and the density effect correction $\delta_F$ that depend on molecular properties. These quantities cannot simply be summed over constituent elements in a compound but should instead be calculated for the material. Currently, we use Bragg's additivity rule to calculate the collision stopping power as well, but this is not a good approximation and should be fixed in the future.

Since charged particles lose their energy on a much shorter distance scale than do neutral particles, not much error should be introduced by neglecting to transport electrons. However, the bremsstrahlung emitted from high-energy electrons and positrons can travel far from the interaction site. Thus, even without a full electron transport mode, one must model bremsstrahlung. We use a thick-target bremsstrahlung (TTB) approximation based on the models in [8] and [7] for generating bremsstrahlung photons, which assumes that the charged particle loses all its energy in a single homogeneous material region.

To model bremsstrahlung using the TTB approximation, we need to know the number of photons emitted by the charged particle and the energy distribution of the photons. These quantities can be calculated by using the continuous slowing down approximation (CSDA). The CSDA assumes that charged particles lose energy continuously along their trajectory with a rate of energy loss equal to the total stopping power, ignoring fluctuations in the energy loss. The approximation is useful for expressing average quantities that describe how charged particles slow in matter. For example, the CSDA range approximates the average path length a charged particle travels as it slows to rest:

$$R(T) = \int_0^T \frac{dT'}{S(T')}. \tag{51}$$

Actual path lengths will fluctuate around $R(T)$. The average number of photons emitted per unit path length is given by the inverse bremsstrahlung mean free path:

$$\lambda_{\text{br}}^{-1}(T, E_{\text{cut}}) = n \int_{E_{\text{cut}}}^{T} \frac{d\sigma_{\text{br}}}{dE} dE = n \frac{Z^2}{\beta^2} \int_{\kappa_{\text{cut}}}^{1} \frac{1}{\kappa} \chi(Z, T, \kappa) d\kappa. \tag{52}$$

The lower limit of the integral in Eq. (52) is nonzero because the bremsstrahlung differential cross section diverges for small photon energies but is finite for photon energies above some cutoff energy $E_{\text{cut}}$. The mean free path $\lambda_{\text{br}}^{-1}(T, E_{\text{cut}})$ is used to calculate the photon number yield, defined as the average number of photons emitted with energy greater than $E_{\text{cut}}$ as the charged particle slows from energy $T$ to $E_{\text{cut}}$. The photon number yield is given by

$$Y(T, E_{\text{cut}}) = \int_{R(E_{\text{cut}})}^{R(T)} \lambda_{\text{br}}^{-1}(T', E_{\text{cut}}) ds = \int_{E_{\text{cut}}}^{T} \frac{\lambda_{\text{br}}^{-1}(T', E_{\text{cut}})}{S(T')} dT'. \tag{53}$$

$Y(T, E_{\text{cut}})$ can be used to construct the energy spectrum of bremsstrahlung photons: the number of photons created with energy between $E_1$ and $E_2$ by a charged particle with initial kinetic energy $T$ as it comes to rest is given by $Y(T, E_1) - Y(T, E_2)$.

The data needed for the TTB approximation is assembled from various sources. The scaled bremsstrahlung cross sections are given by Seltzer and Berger [9] for $Z = 1 - 100$ for incident electron kinetic energies between 1 keV and 10 GeV and for 30 reduced photon energies for each electron energy. This is generally considered the most reliable data available and is generated by using a combination of various theoretical results and interpolation. Both the collision and radiative stopping powers are pulled from the NIST ESTAR database [10], which provides stopping powers for electrons in various materials (including $Z = 1 - 98$) for energies between 1 keV and 10 GeV.

In order to simulate the emission of bremsstrahlung photons, the total stopping power and bremsstrahlung differential cross section for positrons and electrons must be calculated for a given material by using Eq. (49) and Eq. (50). These quantities are used to build the tabulated bremsstrahlung energy PDF and CDF for that material for each incident energy $T_k$ on the energy grid. The following algorithm is then applied to sample the photon energies:

1. For an incident charged particle with energy $T$, sample the number of emitted photons as
$$N = \lfloor Y(T, E_{\text{cut}}) + \xi_1 \rfloor.$$

2. Rather than interpolate the PDF between indices $k$ and $k+1$ for which $T_k < T < T_{k+1}$, which is computationally expensive, use the composition method and sample from the PDF at either $k$ or $k+1$. Using linear interpolation on a logarithmic scale, the PDF can be expressed as
$$p_{\text{br}}(T, E) = \pi_k p_{\text{br}}(T_k, E) + \pi_{k+1} p_{\text{br}}(T_{k+1}, E),$$
where the interpolation weights are
$$\pi_k = \frac{\ln T_{k+1} - \ln T}{\ln T_{k+1} - \ln T_k}, \quad \pi_{k+1} = \frac{\ln T - \ln T_k}{\ln T_{k+1} - \ln T_k}.$$
Sample either the index $i = k$ or $i = k+1$ according to the point probabilities $\pi_k$ and $\pi_{k+1}$.

3. Determine the maximum value of the CDF $P_{\text{br,max}}$.

4. Sample the photon energies using the inverse transform method with the tabulated CDF $P_{\text{br}}(T_i, E)$, i.e.,

$$E = E_j \left[ (1 + a_j) \frac{\xi_2 P_{\text{br,max}} - P_{\text{br}}(T_i, E_j)}{E_j p_{\text{br}}(T_i, E_j)} + 1 \right]^{\frac{1}{1+a_j}},$$

where the interpolation factor $a_j$ is given by

$$a_j = \frac{\ln p_{\text{br}}(T_i, E_{j+1}) - \ln p_{\text{br}}(T_i, E_j)}{\ln E_{j+1} - \ln E_j}$$

and $P_{\text{br}}(T_i, E_j) \leq \xi_2 P_{\text{br,max}} \leq P_{\text{br}}(T_i, E_{j+1})$.

We ignore the range of the electron or positron; in other words, the bremsstrahlung photons are produced in the same location that the charged particle was created. The direction of the photons is assumed to be the same as the direction of the incident charged particle, which is a reasonable approximation at higher energies when the bremsstrahlung radiation is emitted at small angles.

# 3 Photon Production

In coupled neutron-photon transport, a source neutron is tracked, and photons produced from neutron reactions are transported after the neutron's history has terminated. Since these secondary photons form the photon source for the problem, it is important to correctly describe their energy and angular distributions as the accuracy of the calculation relies on the accuracy of this source. Both the photon production cross sections and the secondary angle and energy distributions for photons produced from neutron reactions are specified as part of the incident neutron sublibraries. Photon production cross sections may be provided either directly or in the form of the photon multiplicity (yield). The photon production cross section for a particular reaction $i$ and incident neutron energy $E$ is defined as

$$\sigma_{\gamma,i}(E) = y_i(E)\sigma_i(E), \tag{54}$$

where $y_i(E)$ is the photon yield corresponding to an incident neutron reaction having cross section $\sigma_i(E)$. If the yield is specified, the photon production cross section can be calculated as the product of the yield and the cross section for the neutron reaction.

The yield of photons during neutron transport is determined as the sum of the photon yields from each individual reaction. In OpenMC, production of photons is treated in an average sense. That is, the total photon production cross section is used at a collision site to determine how many photons to produce rather than the photon production from the reaction that actually took place. This is partly done for convenience but also because the use of variance reduction techniques such as implicit capture make it difficult in practice to directly sample photon production from individual reactions.

In OpenMC, secondary photons are created after a nuclide has been sampled in a neutron collision. The expected number of photons produced is

$$n = w\frac{\sigma_\gamma(E)}{\sigma_T(E)}, \tag{55}$$

where $w$ is the weight of the neutron, $\sigma_\gamma$ is the photon production cross section for the sampled nuclide, and $\sigma_T$ is the total cross section for the nuclide. $\lfloor n \rfloor$ photons are created with an additional photon produced with probability $n - \lfloor n \rfloor$. Next, a reaction is sampled for each secondary photon. The probability of sampling the $i$th reaction is given by $\sigma_{\gamma,i}(E)/\sum_j \sigma_{\gamma,j}(E)$, where $\sum_j \sigma_{\gamma,j} = \sigma_\gamma$ is the total photon production cross section. The secondary angle and energy distributions associated with the reaction are used to sample the angle and energy of the emitted photon.

# 4 Validation

Both the photon physics and photon production implementations in OpenMC have been compared with MCNP6. Two test cases were studied: a monoenergetic, isotropic photon point source in an infinite medium, used to identify differences in photon physics, and a monoenergetic, monodirectional neutron source directed down a thin, infinitely long cylinder, used to expose any differences in the photon production implementations.

The same data was used with OpenMC and MCNP whenever possible to simplify comparisons. For photon transport, the eprdata12 library was used for the MCNP calculations, while OpenMC used a combination of the eprdata12 library, bremsstrahlung differential cross sections from Seltzer and Berger, and stopping powers from the NIST ESTAR database. The bremsstrahlung cross section data used in MCNP also comes from Seltzer and Berger; however, MCNP internally calculates the collision and radiative stopping powers. Both OpenMC and MCNP used neutron cross section data from the ENDF71x ACE library that is distributed with MCNP6.

## 4.1 Point Source in an Infinite Geometry

The test case used to study the photon physics models consists of a monoenergetic, isotropic point source of $10^7$ photons at the center of a large sphere. The sphere is made up of a single material and has a radius of $10^9$ cm, large enough to assume that no particles are leaked from the geometry. The photon cutoff energy is set to 1 keV. Calculations were performed for source energies of 0.1, 1, 10, and 100 MeV for various materials, and the photon spectrum was tallied.

Figs. 1 to 7 show the energy spectra from MCNP6 and OpenMC with the relative error plotted alongside the uncertainties. For the most part the results show reasonably good agreement, particularly at low energies that are more important for reactor calculations, but there are some notable discrepancies.

One of the main differences is related to the collision stopping powers used in the TTB approximation in OpenMC. The stopping powers from the NIST ESTAR database are calculated for each element using by default the material density at standard temperature and pressure. When the density of a material in a problem is different from the density used in the ESTAR

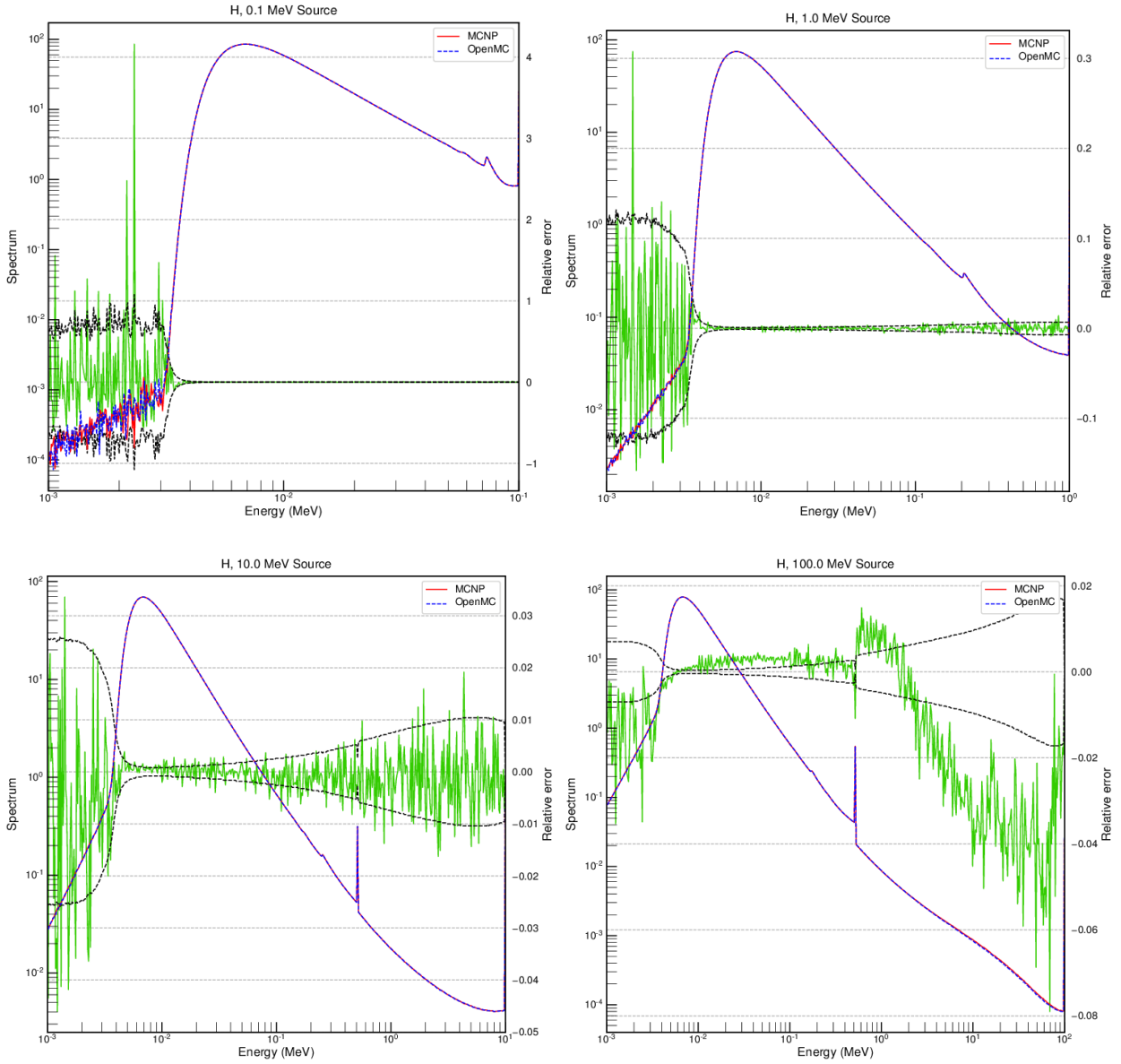


Figure 1: Photon energy spectrum in an infinite geometry for hydrogen at a density of $8.3748 \times 10^{-5}$ g/cm$^3$. The spectra calculated with OpenMC and MCNP6 are plotted along the left axis. The relative error between the spectra is plotted in green along the right axis with the uncertainties in black.

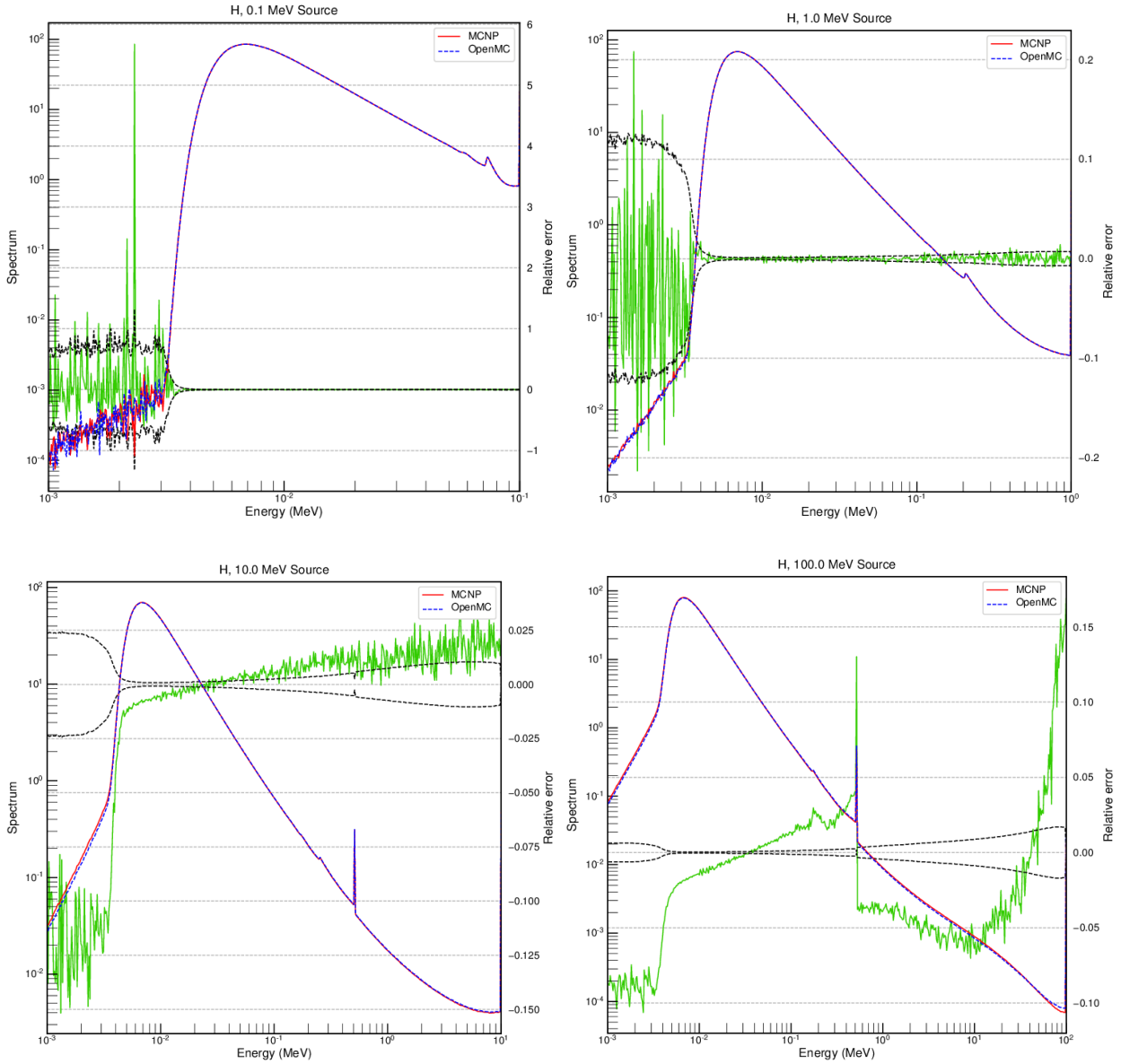


Figure 2: Photon energy spectrum in an infinite geometry for hydrogen at a density of 1 g/cm$^3$. The spectra calculated with OpenMC and MCNP6 are plotted along the left axis. The relative error between the spectra is plotted in green along the right axis with the uncertainties in black..

database, the NIST data will be a poor approximation. The reason is that the collision stopping power is a function of certain quantities, such as the mean excitation energy and particularly the density effect correction, that depend on material properties. The density effect correction accounts for the polarization of atoms near the path of the charged particle and is a function of the composition and density of the material. Stopping powers for compounds are calculated from the elemental data with Bragg's additivity rule, which introduces additional error. Data for constituent elements in a compound cannot simply be summed together; instead, these quantities must be calculated for the material.

Fig. 1 and Fig. 2 highlight the problems with the current treatment. Fig. 1 shows the energy spectrum for a photon source in hydrogen with a density of $1.3313 \times 10^{-3}$ g/cm$^3$, at which the NIST data is calculated, while Fig. 2 shows the results for the same model but with a much higher density of 1 g/cm$^3$. For 0.1 and 1 MeV sources, there is good agreement between the OpenMC and MCNP results in both cases. When the source energy is increased to 10 MeV, there is still no discernible difference between the results for the model where hydrogen is at the density used in the NIST calculations. For the higher density model, however, the low end of the spectrum that is formed primarily from bremsstrahlung is underestimated by $10-15\%$ in OpenMC. This is expected because MCNP accounts for the density effect correction, while OpenMC does not. Similar results are observed for the 100 MeV source.

Even when the material density used to calculate ESTAR stopping powers is used in the model, there are discrepancies between the results, particularly for high source energies. These differences are likely related to either differences in the TTB approximation or the model used for sampling the energy of the electron and positron created in pair production. Pair production is the dominant interaction at high energies and is more important for high-Z elements. For example, it starts to dominate over Compton scattering above $\sim$ 80 MeV in hydrogen but above $\sim$ 4 MeV in uranium. Modeling this interaction accurately is important because the charged particles go on to lose their energy as bremsstrahlung. Unfortunately, little documentation is available on how MNCP models either bremsstrahlung or pair production, so it is difficult to determine whether their methods are more accurate and to verify the cause of these discrepancies with certainty.

Fig. 3 shows the spectrum for oxygen. For high-energy sources, OpenMC slightly underestimates the low end of the spectrum and underestimates the high end of the spectrum by up to 15%. One possible cause of the bias in the OpenMC results is the different treatment of positrons in the TTB approximation. While OpenMC has a separate positron treatment, MCNP uses the same cross sections and stopping powers for both electrons and positrons. The bremsstrahlung yield of positrons approaches that of electrons for high incident particle energies but is smaller at lower energies. The difference is also more pronounced for higher-Z elements. This means the bremsstrahlung spectrum will be lower for a calculation that includes both positrons and electrons than it would be if the positrons were treated as electrons and that the difference would be larger for elements with a higher atomic number. This trend is observed in Figs. 4 to 6: for a 10 MeV source the difference at the low end of the spectrum grows to 3–4% in iron to 7–9% in lead and 8–10% in uranium.

For the 100 MeV source, the difference in the high end of the spectrum is even greater and increases from 15% in oxygen to 40% in uranium. This may be due to differences in pair production, TTB, or interpolation methods. However, since it is observed only at very high energies and the spectrum is very low at this point, it will likely be relatively unimportant.

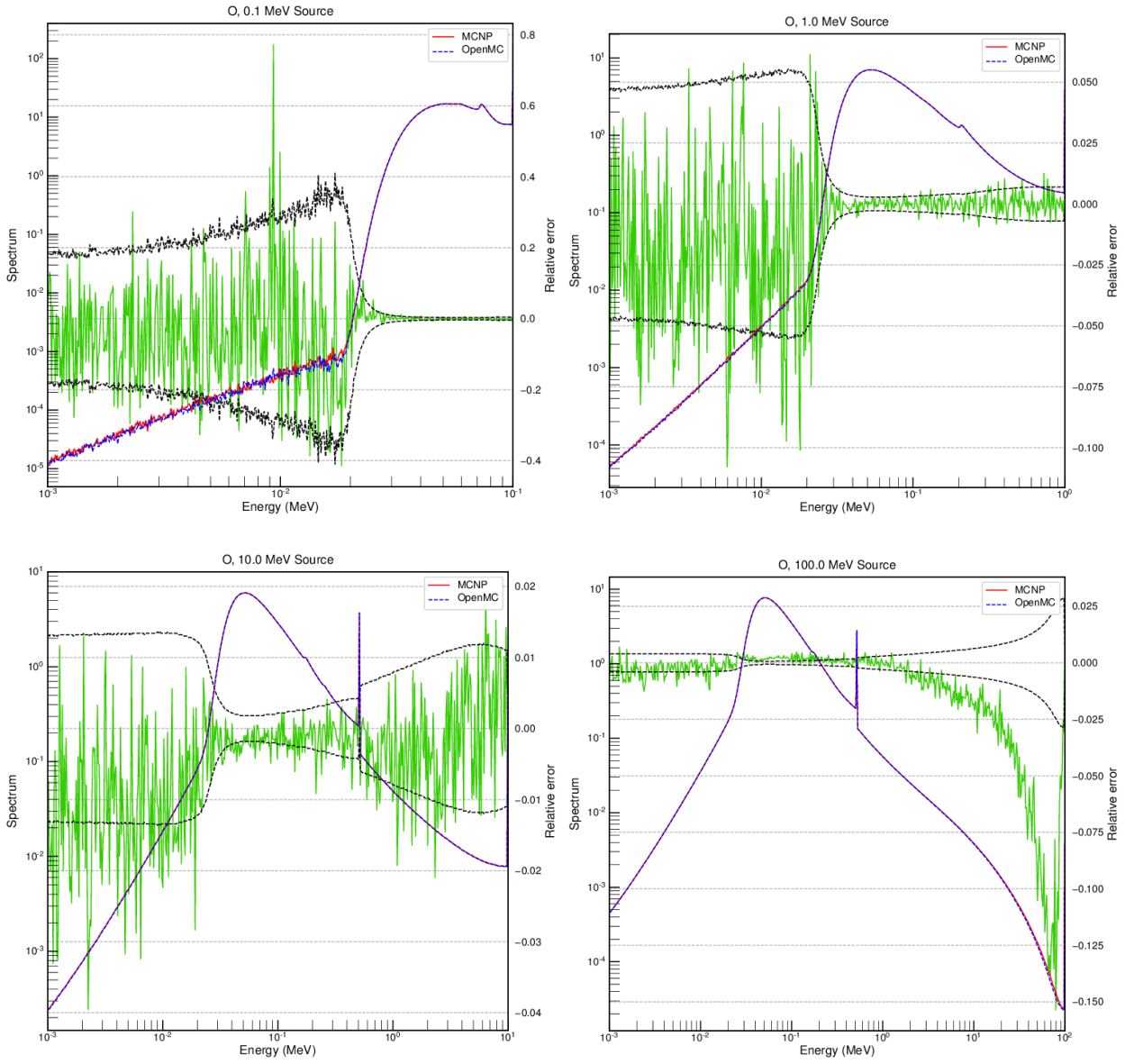


Figure 3: Photon energy spectrum in an infinite geometry for oxygen at a density of $1.3315 \times 10^{-3}$ g/cm$^3$. The spectra calculated with OpenMC and MCNP6 are plotted along the left axis. The relative error between the spectra is plotted in green along the right axis with the uncertainties in black.

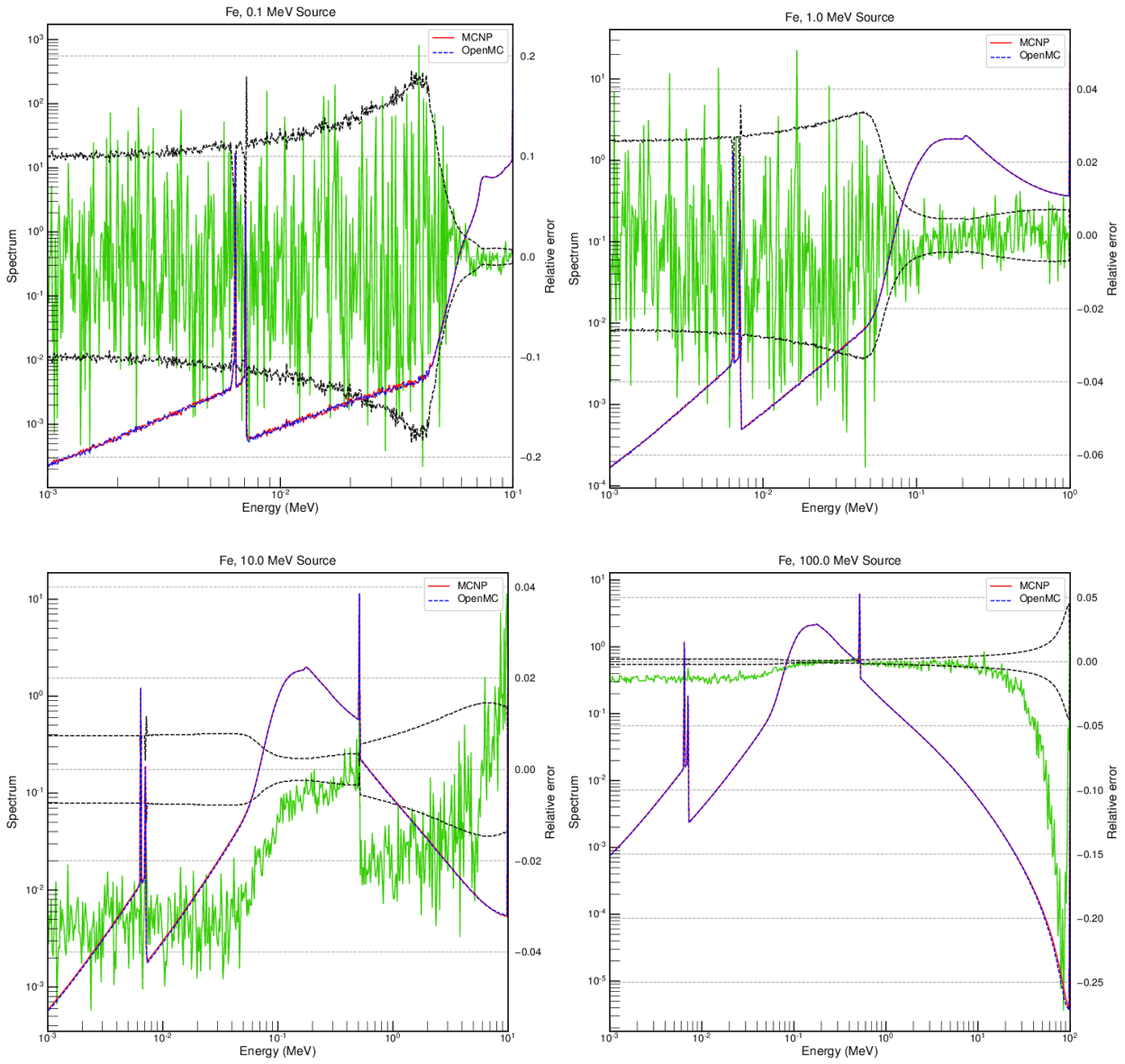


Figure 4: Photon energy spectrum in an infinite geometry for iron at a density of 7.874 g/cm$^3$. The spectra calculated with OpenMC and MCNP6 are plotted along the left axis. The relative error between the spectra is plotted in green along the right axis with the uncertainties in black.

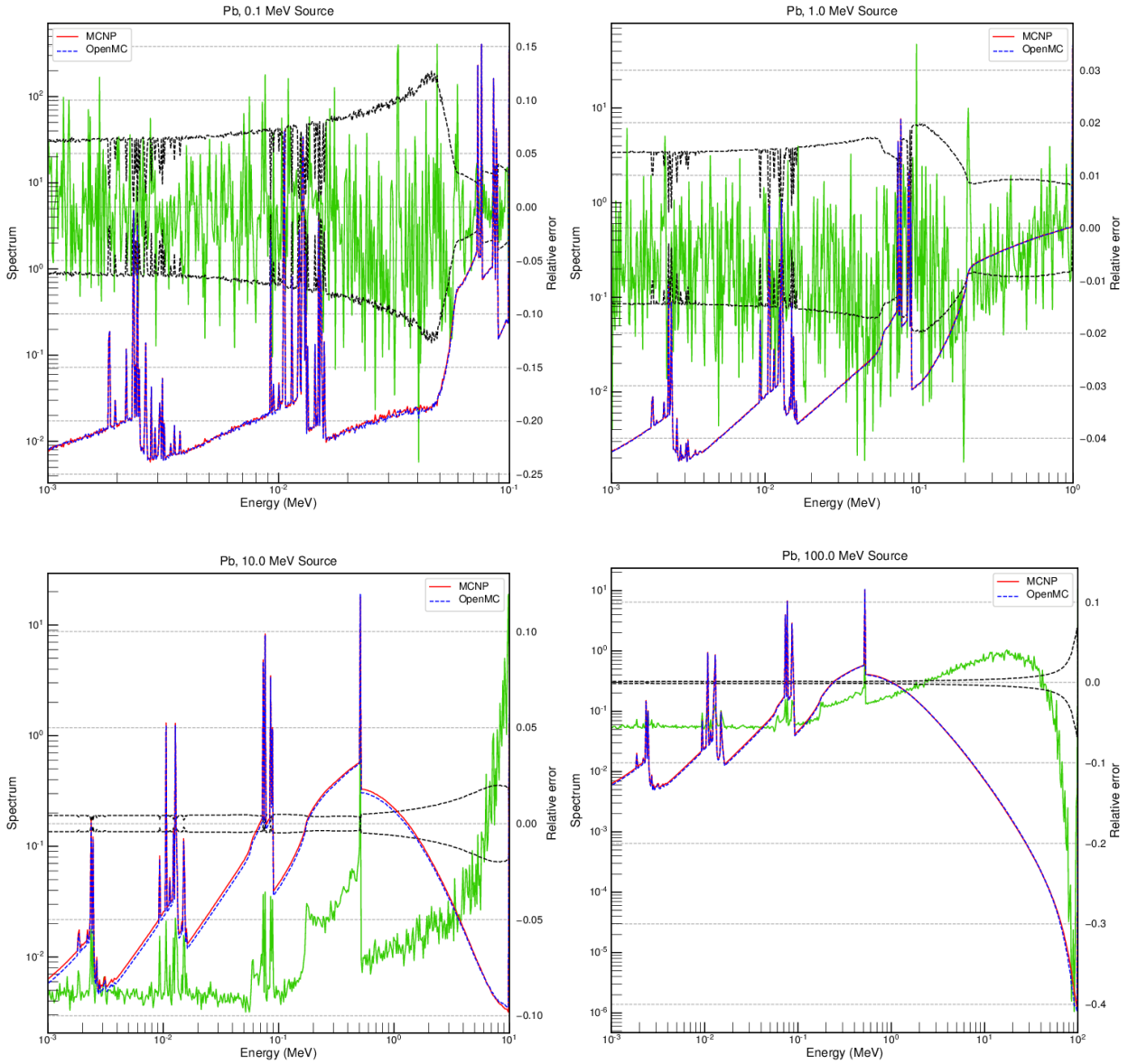


Figure 5: Photon energy spectrum in an infinite geometry for lead at a density of 11.35 g/cm$^3$. The spectra calculated with OpenMC and MCNP6 are plotted along the left axis. The relative error between the spectra is plotted in green along the right axis with the uncertainties in black.

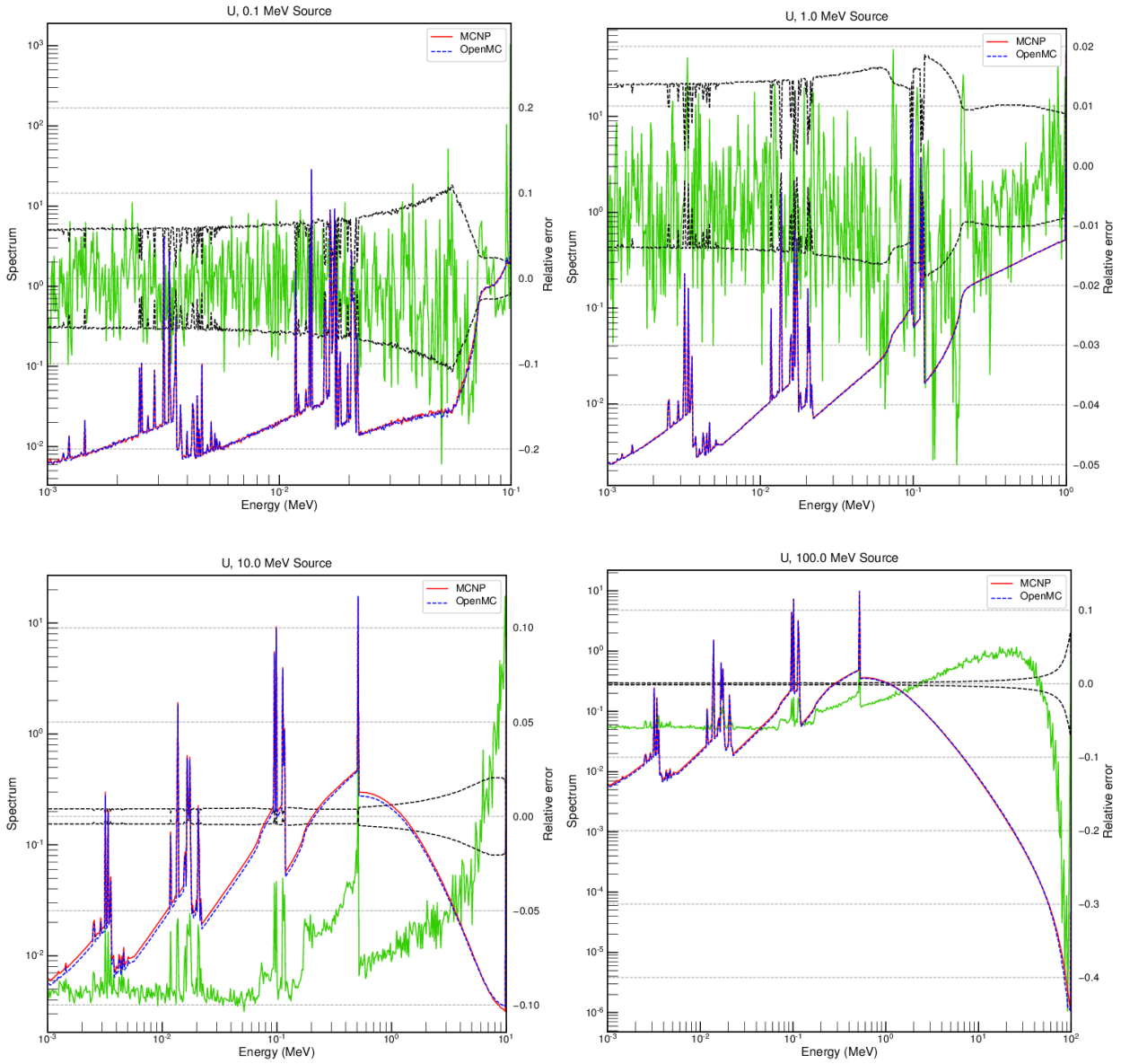


Figure 6: Photon energy spectrum in an infinite geometry for uranium at a density of 18.95 g/cm$^3$. The spectra calculated with OpenMC and MCNP6 are plotted along the left axis. The relative error between the spectra is plotted in green along the right axis with the uncertainties in black.

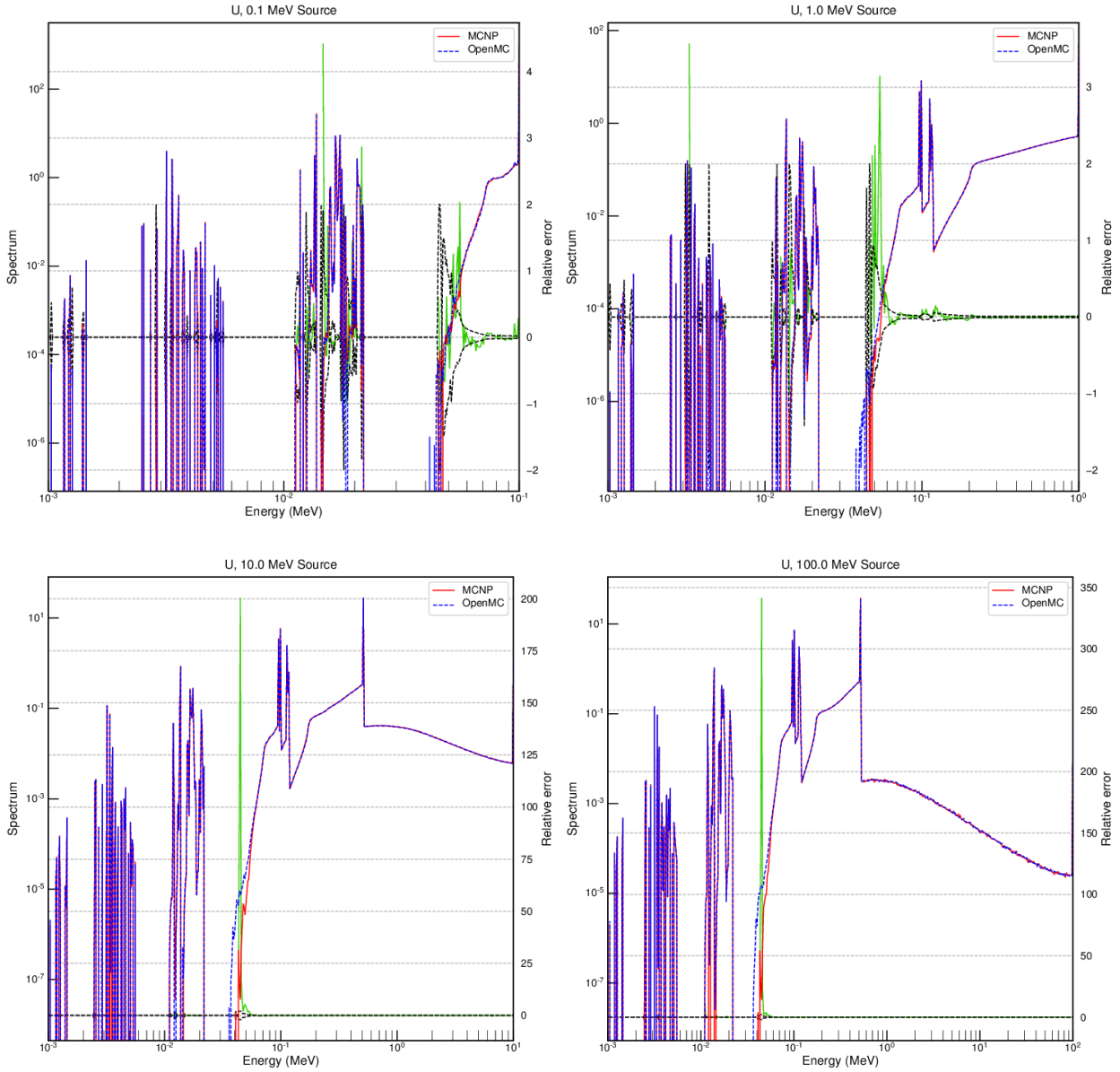


Figure 7: Photon energy spectrum in an infinite geometry for uranium at a density of 18.95 g/cm$^3$. Rather than using the TTB approximation to treat charged particles, local energy deposition is assumed. The spectra calculated with OpenMC and MCNP6 are plotted along the left axis. The relative error between the spectra is plotted in green along the right axis with the uncertainties in black.

The spectrum for uranium is shown in Fig. 6. For comparison, Fig. 7 shows the spectrum for uranium for a calculation in which the local energy deposition option is used instead of bremsstrahlung treatment; that is, energy from charged particles is assumed to be deposited locally, and no photons from bremsstrahlung are created. The results show near-perfect agreement, confirming that any discrepancies come from differences in the models used for charged particles. The one large discrepancy around 40 keV results from a small difference within the procedure for Doppler broadening of Compton-scattered photons: in OpenMC, the maximum value of the cumulative distribution function is interpolated at $p_{z,max}$, while MCNP uses the lower bounding value on the grid.

Overall, the results show reasonably good agreement in the energy range that is relevant for reactor calculations. The cases where the results diverge are primarily for very high energy photons that are not energetically possible in a reactor.

### 4.2 Broomstick Problem

To identify any problems in the photon production implementation in OpenMC, a so-called Broomstick model was used to compare the results to MCNP. The geometry consists of a cylinder with radius $1 \times 10^{-6}$ cm and length $1 \times 10^{9}$ cm (i.e., thin and infinitely long) made of of a single material. A monoenergetic, monodirectional neutron source is directed down the length of the cylinder. Any secondary particles produced escape before they have a chance to interact, so the energy distribution of secondary photons produced in neutron reactions can be observed without any contribution from other photon interactions. The photon current is tallied over the surface of the cylinder. The comparisons were carried out for a few different source energies and many different nuclides. Some representative plots are shown in Fig. 8, with the relative error and the uncertainties plotted alongside the spectra. OpenMC results are consistent with MCNP results for all of the calculations performed so far.

## 5 Acknowledgments

This material was based upon work supported by the U.S. Department of Energy, Office of Science, Advanced Scientific Computing Research, under Contract DE-AC02-06CH11357.

## References

[1] N. J. Carron, *An Introduction to the Passage of Energetic Particles through Matter*. Taylor & Francis, 2007.

[2] H. Kahn, "Applications of Monte Carlo," Tech. Rep. RM-1237-AEC, The Rand Corporation, 1956.

[3] L. Koblinger, "Direct sampling from the Klein-Nishina distribution for photon energies above 1.4 MeV," *Nucl. Sci. Eng.*, vol. 56, no. 2, pp. 218–219, 1975.

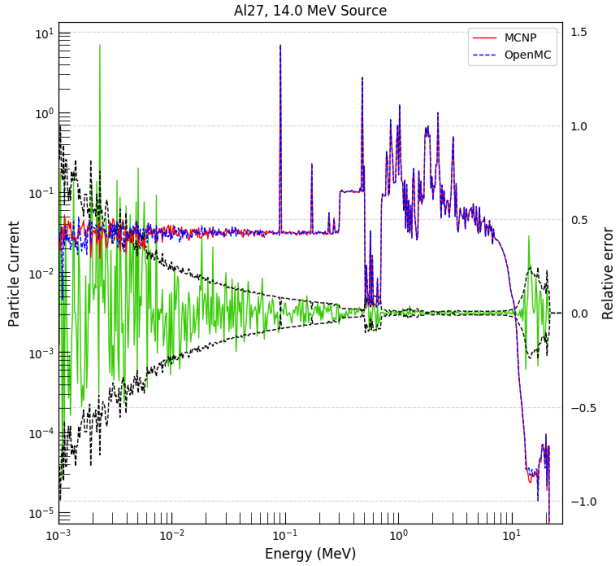


(a) $^{27}$Al at 2.6989 g/cm$^3$.

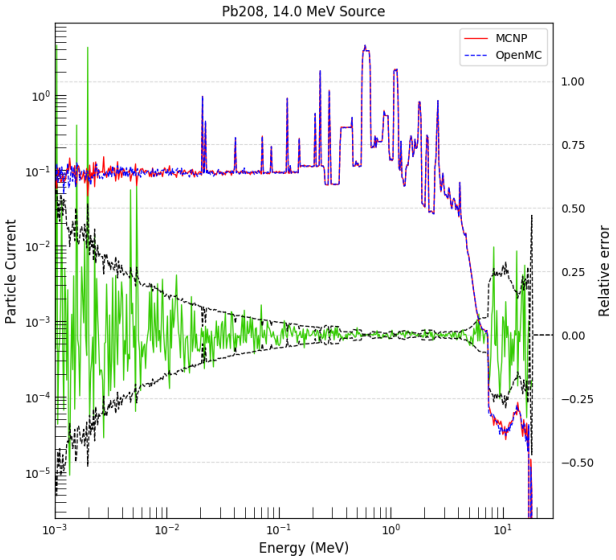


(b) $^{208}$Pb at 11.35 g/cm$^3$.

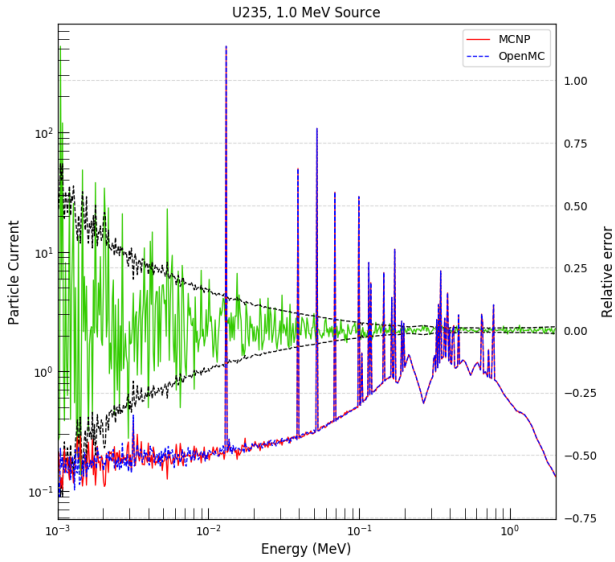


(c) $^{235}$U at 18.95 g/cm$^3$.

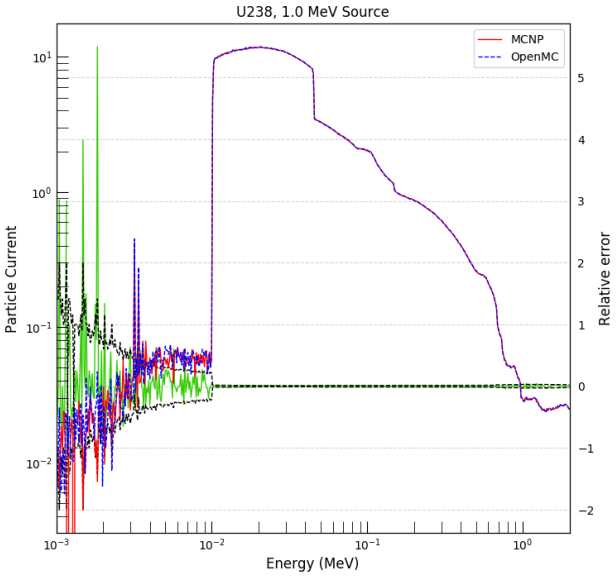


(d) $^{238}$U at 18.95 g/cm$^3$.

Figure 8: Secondary photon spectrum for the Broomstick problem for four different nuclides. A 14 MeV neutron source was used to generate the results in the top two figures, and a 1 MeV neutron source was used to generate the results in the bottom two figures. The current calculated with OpenMC and MCNP6 are plotted along the left axis. The relative error between the spectra is plotted in green along the right axis with the uncertainties in black.

[4] A. Sood, "Doppler energy broadening for incoherent scattering in MCNP5, part I," Tech. Rep. LA-UR-04-0487, Los Alamos National Laboratory, 2004.

[5] A. Sood and M. C. White, "Doppler energy broadening for incoherent scattering in MCNP5, part II," Tech. Rep. LA-UR-04-0488, Los Alamos National Laboratory, 2004.

[6] F. Biggs, L. Mendelsohn, and J. Mann, "Hartree-Fock Compton profiles for the elements," *Atomic Data and Nuclear Data Tables*, vol. 16, no. 3, pp. 201–309, 1975.

[7] T. Kaltiaisenaho, "Implementing a photon physics model in Serpent 2," Master's thesis, Aalto University, May 2016.

[8] F. Salvat, J. M. Fernández-Varea, and J. Sempau, *PENELOPE-2011: A Code System for Monte Carlo Simulation of Electron and Photon Transport*. OECD-NEA, Issy-les-Moulineaux, France, 2011.

[9] S. M. Seltzer and M. J. Berger, "Bremsstrahlung energy spectra from electrons with kinetic energy 1 keV-10 GeV incident on screened nuclei and orbital electrons of neutral atoms with Z = 1-100," *Atomic Data and Nuclear Data Tables*, vol. 35, no. 3, pp. 345–418, 1986.

[10] "ESTAR stopping power and range tables for electrons." `https://www.physics.nist.gov/PhysRefData/Star/Text/ESTAR.html`.


**Mathematics and Computer Science Division**
Argonne National Laboratory
9700 South Cass Avenue, Bldg. 240
Argonne, IL 60439

www.anl.gov